Reaction Chemistry & Engineering

ROYAL SOCIETY OF CHEMISTRY

REVIEW

View Article Online
View Journal | View Issue

Cite this: *React. Chem. Eng.*, 2021, **6**, 612

Electrochemical reduction of CO_2 towards multi-carbon products *via* a two-step process

Xianbiao Fu, Jiahao Zhang and Yijin Kang *

Received 1st January 2021,
Accepted 5th February 2021

DOI: 10.1039/d1re00001b

rsc.li/reaction-engineering

The electrochemical conversion of carbon dioxide (CO_2) towards clean fuels and chemicals powered by renewable energy is a promising strategy to realize the closing of the loop of carbon footprint. However, the direct reduction of CO_2 to multi-carbon (C_{2+}) products suffers from low activity in non-alkaline electrolyte or electrolyte degradation problem caused by carbonate formation in alkaline electrolyte. The two-step process for CO_2 electrocution can circumvent such problems by converting CO_2 to CO (the first step) in the non-alkaline electrolyte and promote the rate of carbon–carbon coupling for CO-to-C_{2+} conversion (the second step) in alkaline electrolytes. We summarize the recent progress of CO-selective catalysts, C_{2+}-selective catalysts, tandem catalysts, and tandem reaction systems, which aim to achieve the efficient production of C_{2+} products with high selectivity. The two-step route of CO_2 reduction pushes the chemical production from environmentally abundant molecules closer to the practical application, offering a promising replacement in the petrochemical industry for chemical production under hydrogen economy in the future.

1. Introduction

The electrochemical carbon dioxide reduction reaction (CO_2RR) is an alternative route for valuable fuels and chemical production with the plummeting cost of renewable electricity.[1–5] In general, CO_2 molecules can be converted into carbon monoxide (CO), methane (CH_4), methanol (CH_3OH), formic acid (HCOOH), ethylene (C_2H_4), ethanol (CH_3CH_2OH), acetate acid (CH_3COOH), propanol (n-$CH_3CH_2CH_2OH$), and chemicals with even longer carbon chains. Among all CO_2RR electrocatalysts, only copper-based catalysts have been shown to have the unique capability to convert CO_2/CO into multicarbon (C_{2+}) products with acceptable selectivities.[6–9] Many efforts have been devoted towards regulating the selectivity of C_{2+} products, such as optimizing crystal facets,[6,10] modifying oxidation state,[11,12] introducing defects,[13] alloying,[14,15] functionalizing the catalyst surface,[16–18] and engineering the electrolyzer.[19,20] However, further improving the selectivity of C_{2+} products suffers from fundamental problems and industrially relevant challenges.

Institute of Fundamental and Frontier Sciences, University of Electronic Science and Technology of China, Chengdu, 610054, China.
E-mail: kangyijin@uestc.edu.cn

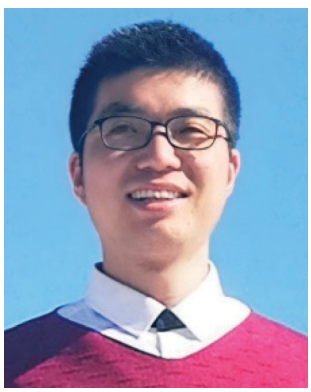

Xianbiao Fu

Xianbiao Fu is a Ph.D. candidate at the University of Electronic Science and Technology of China, under the supervision of Prof. Yijin Kang. He was a visiting graduate student at Northwestern University for two years and Johns Hopkins University for one year. He obtained his B.S. degree from Central South University in 2016. His research focuses on the electroreduction of CO_2/CO into fuels/chemicals, controllable synthesis of model nanocatalysts, and flow-cell/MEA reactor design for electrochemical systems.

Jiahao Zhang

Jiahao Zhang received his B.S. degree from Southwest Petroleum University in 2019. He is currently working on his M.S. degree under the supervision of Prof. Yijin Kang at the Institute of Fundamental and Frontier Sciences, University of Electronic Science and Technology of China. His research interests include carbon dioxide reduction reaction (CO_2RR), oxygen evolution reaction (OER), and polymer electrolyte membrane (PEM) electrolyzers.

Recently, some progress has been made to improve the selectivity and formation rates of C_{2+} products *via* the use of alkaline electrolytes; however, the CO_2 electrolyzer is an electrolyte-consuming device due to the formation of carbonate.[21,22] In addition, the energy required to regenerate CO_2 from aqueous carbonate is much larger than $|\Delta G^\circ|$, making CO_2RR in alkaline electrolytes an energy-expensive device. A more detailed discussion of the problem of carbonate formation in alkaline CO_2 electrolyzer can be seen in the comments from Matthew W. Kanan.[22] Therefore, a two-step route for CO_2 electrochemical reduction to C_{2+} products was proposed to circumvent the carbonate formation in an alkaline CO_2 electrolyzer.[23] As shown in Fig. 1, CO_2 was first reduced to CO in a non-alkaline electrolyte and the produced CO was subsequently converted into C_{2+} products as the second step in an alkaline electrolyte with significantly improved C_{2+} selectivity and activity. There is no problem of carbonate formation between CO and hydroxide, and the use of alkaline electrolytes can indeed improve the reactivity of CO in electrolysis. The two-step electroreduction of CO_2 to C_{2+} products with high selectivity and production rates of industrial relevance provides an alternative route for converting CO_2 to fuels and chemicals.[24,25]

The electrochemical CO reduction reaction (CORR) to C_{2+} products is the key to the two-step conversion process, which enhances the reaction rate and selectivity. In addition to the fact that the CORR process can be carried out in alkaline electrolytes to reduce the overpotential, CORR holds several other advantages over direct CO_2RR.[25] It is known that CO is the key intermediate to C_{2+} products in CO_2 electrolysis. The direct use of CO as the reactant can increase C–C coupling rates to improve the formation rates of C_{2+} products.[6,23] Moreover, the inherent reactivity of CO is higher than that of CO_2. It is proved that for C_{2+} production from CO, the reactant higher current densities can be achieved at lower overpotential compared to from CO_2 as the reactant.[24] The adsorption of CO on the catalyst surface is stronger than CO_2, which helps to suppress the competitive hydrogen evolution reaction (HER), which in turn is beneficial for vastly improving the current efficiency for C_{2+} product formation.[26] The electrochemical reduction of CO_2 to CO has been achieved with high faradaic efficiencies (FE) at high current densities, which provides sustainable feedstock (CO_2-derived CO) in CO electrolysis.

A two-step route for CO_2 electroreduction can be achieved *via* the tandem electrode structure, bimetallic catalysts, and tandem reaction systems, as shown in Fig. 2. Tandem catalysis strategy was obtained from thermal heterogeneous catalysis to break the linear scaling relations of the binding strength for intermediates in CO_2RR.[27,28] The tandem electrode structure is achieved by two different catalysts for CO_2-to-CO and CO-to-C_{2+} production, respectively. Moreover, the development of the catalyst with two sites for the production of CO and C_{2+}, respectively, has also attracted considerable attention. For example, bifunctional catalysts enable *in situ* CO production and consumption, making the high-cost gas separation step unnecessary. As shown in Fig. 2b, tandem reaction systems are also a promising alternative to be explored. Many research efforts have been focused on the second step with pure CO as the feedstock but the interdependence of both steps is rarely considered. From the angle of either catalysis science or electrolyzer engineering, there is plenty of room for tandem catalysis to improve the selectivity and production rate of C_{2+} products. This review offers a perspective regarding the two-step route for the electrochemical reduction of CO_2 to C_{2+} products.

2. The first step: reduce CO_2 to CO

The electrochemical reduction of CO_2 to CO with high selectivity and current density is a prerequisite for the two-step route of CO_2 electroreduction. In general, Au, Ag, and their alloys are commonly used electrocatalysts for the specific reduction of CO_2 to CO at low temperature.[29–31] These catalysts with medium hydrogen overpotential and weak CO adsorption can break the carbon–oxygen bond in CO_2 and allow the produced CO to readily desorb from the surface of the catalysts. Although many strategies have been developed for improving the properties of noble metal catalysts, such as nanostructuring,[32,33] alloying,[34,35] phase engineering,[30] grain boundary engineering,[29] and crystal facet engineering,[36,37] the practical applications of noble metal catalysts are still hindered by the high cost and scarcity. However, developing the electrocatalysts based on earth-abundant elements for the electroreduction of CO_2 to CO remains challenging.

Atomically dispersed earth-abundant metals anchored in nitrogen-doped carbon matrices (M–N–C) are promising candidates for CO_2-to-CO conversion, with projected superior activity and selectivity.[38–40] Wang and co-works reported a facile ion adsorption process to synthesize Ni single-atom

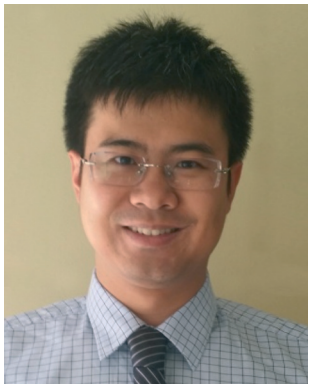

Yijin Kang

Yijin Kang is currently a Professor at the Institute of Fundamental and Frontier Sciences, University of Electronic Science and Technology of China. He was also a Visiting Professor at the Institute for Sustainability and Energy, Northwestern University and an Adjunct Professor at the Department of Chemical Engineering, University of Illinois at Chicago, United States. He received his B.S. (2005) at Fudan University, Ph. D. (2012) from the University of Pennsylvania, and did postdoctoral research at Argonne National Laboratory. His research focuses on energy conversion and storage, including fuel cell technology, battery technology, and chemical upgrade using catalytic processes such as hydrogenation, selective oxidation, CO_2/CO reduction, and ammonia synthesis.

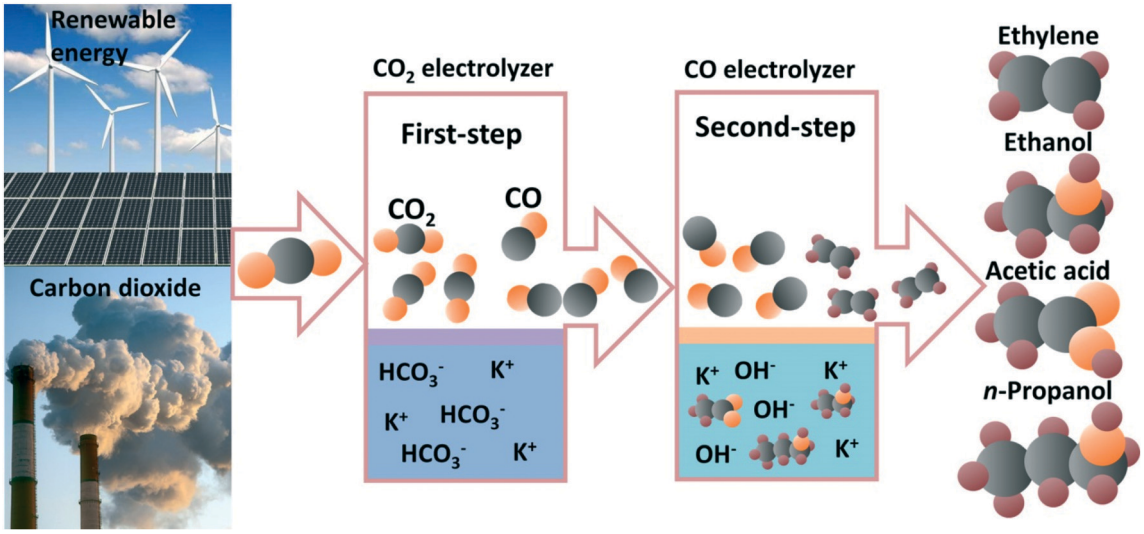

Fig. 1 Schematic illustration of the two-step CO_2 electrochemical reduction to multicarbon products.

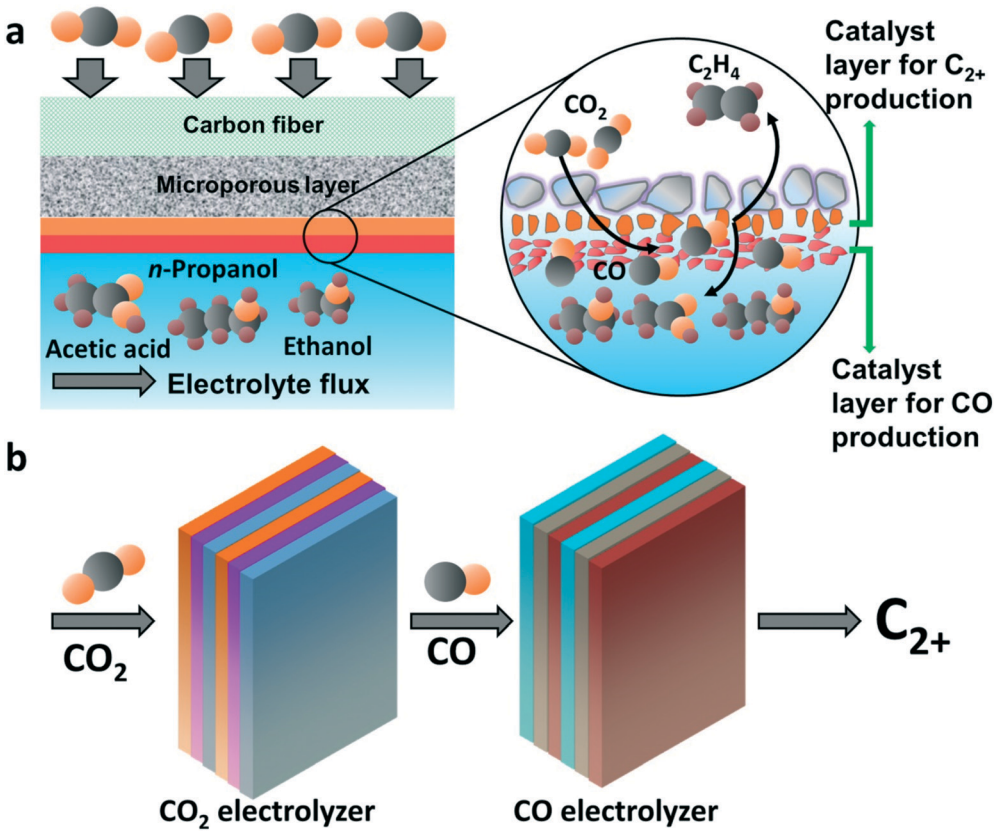

Fig. 2 The two-step CO_2 electroreduction strategies. (a) Tandem catalysts reduce CO_2 to multicarbons. (b) Tandem reaction systems for converting CO_2 to multicarbons.

catalysts on commercial carbon black (Ni-NCB) (Fig. 3a).[41] The CO_2RR tested in an anion membrane electrode assembly (MEA) (Fig. 3b) demonstrated that the Ni-NCB catalyst exhibited a current density up to 130 mA cm^{-2} (Fig. 3c) and nearly 100% CO faradaic efficiency ($FE_{(CO)}$) (Fig. 3d). As shown in Fig. 3e, a maximum CO/H_2 ratio of 113.8 was achieved at a current density of 74 mA cm^{-2}. The results reveal that earth-abundant catalysts with remarkable CO production performance are promising to replace the noble metal catalysts (*e.g.*, Au and Ag). Liu and co-workers prepared a single Ni-atom catalyst by pyrolyzing a mixture of amino acid, melamine, and nickel acetate in argon.[42] Aberration-

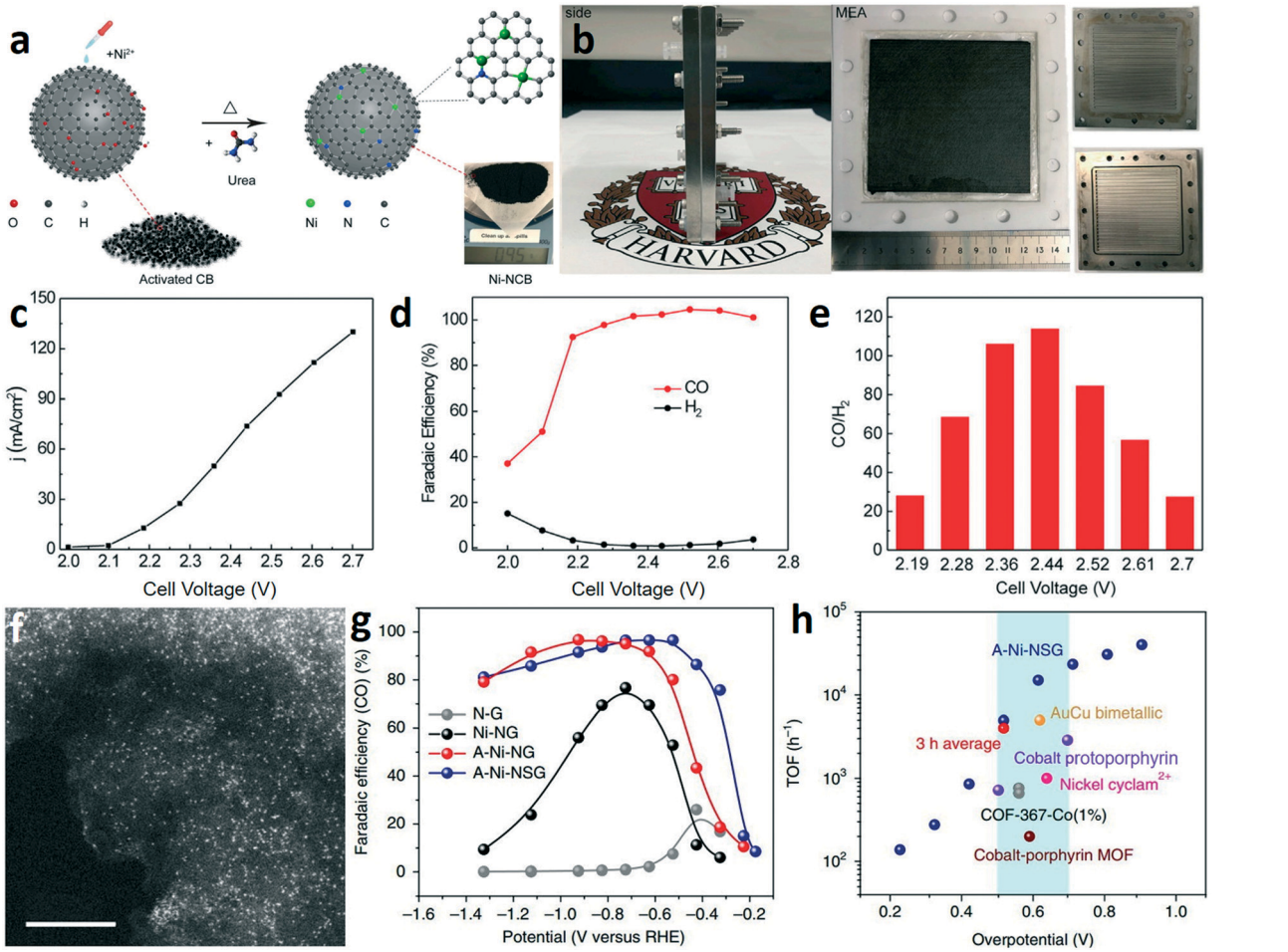

Fig. 3 (a) Schematic illustration for the formation process of Ni-NCB. (b) Photographs of the membrane electrode assembly and individual cell components. (c–e) The current densities (c), the corresponding CO faradaic efficiency (d), and the CO/H_2 ratio (e) of Ni-NCB. Reproduced with permission.[41] Copyright 2019, Elsevier. (f) HAADF-STEM image of A-Ni-NG, scale bar: 5 nm. (g) CO faradaic efficiency at various applied potentials. (h) TOF of A-Ni-NSG compared with those of other state-of-the-art CO_2-to-CO catalysts. Reproduced with permission.[42] Copyright 2018, Nature Publishing Group.

corrected high-angle annular dark-field scanning transmission electron microscopy (HAADF-STEM) was used to confirm the dispersion of Ni atoms on the graphene (Fig. 3f). In a traditional H-type electrolyzer, the A-Ni-NSG (the Ni atoms atomically dispersed on N-doped graphene prepared by the addition of L-cysteine) catalyst achieved a maximum $FE_{(CO)}$ of about 97% at about −0.5 V (*vs.* RHE) (Fig. 3g). Noteworthily, the A-Ni-NSG catalyst exhibited a high intrinsic CO_2 reduction activity. The turnover frequency (TOF) of A-Ni-NSG reached 14 800 h^{-1} at an overpotential of 0.61 V (Fig. 3h), which is much larger than that of some noble metal catalysts and molecular catalysts. *Operando* X-ray absorption and photoelectron spectroscopy reveal that the monovalent Ni(I) atomic center as the active site can reduce the energy barrier for CO_2RR *via* spontaneous charge transfer, which is responsible for the high intrinsic CO_2 reduction activity.

Molecular catalysts, such as metal phthalocyanine (MPc) and metal tetraphenylporphyrin (MTPP), have attracted considerable interests as electrocatalysts for CO_2-to-CO conversion due to their uniform and tunable active sites, which are beneficial for revealing the structure–activity relationships and in turn to guide the rational design of the catalyst.[43–45] Due to their poor conductivity, the molecular catalysts are usually supported on conductive materials to afford higher current densities.[46] The selectivity and activity of the molecular catalyst can be regulated *via* the metal center, ligands, and ligand substituents. As shown in Fig. 4a, Liang and co-workers designed a series of nickel phthalocyanine molecules anchored on the side-walls of carbon nanotubes to control the performance of CO_2 reduction by pendant group functionalization.[47] Among the nickel phthalocyanine (NiPc) molecularly dispersed electrocatalysts (MDEs), NiPc-OMe achieved a CO selectivity of >99% in a wide current density range (*i.e.*, −10 to −400 mA cm^{-2}), which outperforms that of the pyrolyzed Ni–N–C catalyst and noble metal catalysts (Fig. 4b). Based on *in situ* X-ray absorption spectroscopy (XAS) and density functional theory (DFT) calculations, the electron-donating groups (–OMe) can increase the electron density on the Ni atoms and hence enhance the Ni–N bond strength to improve their electrochemical stability in CO_2 electrolysis, which is the reverse for the electron-

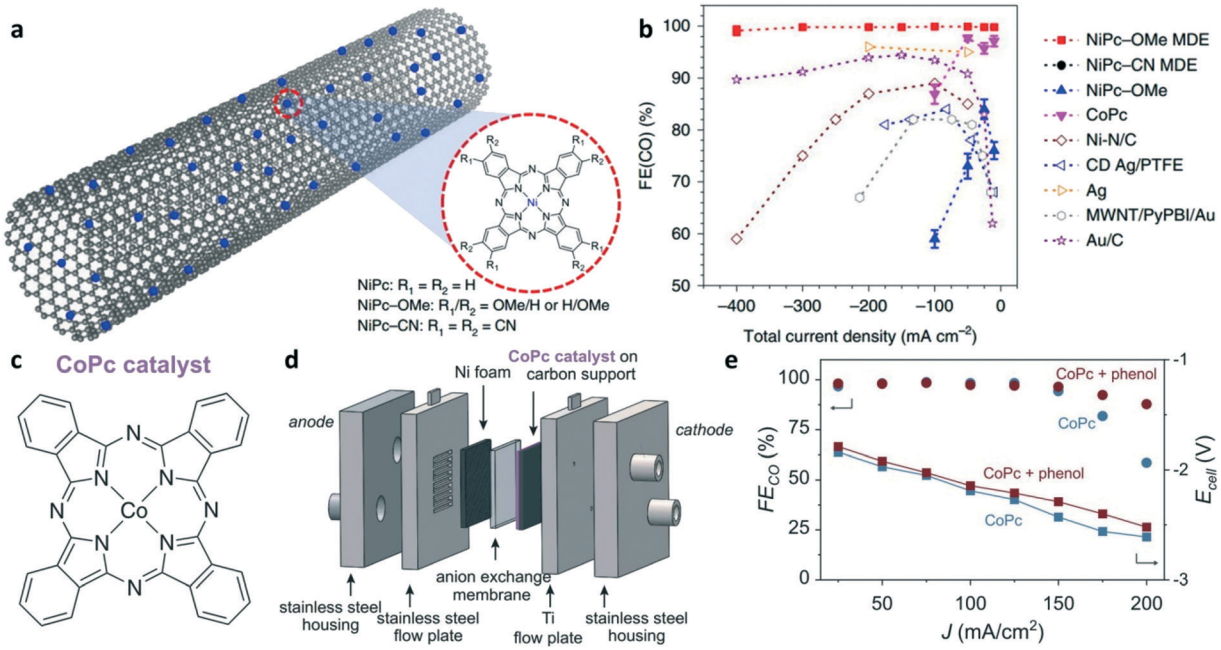

Fig. 4 (a) Schematic illustration for NiPc molecules anchored on the CNTs. (b) $FE_{(CO)}$ of NiPc MDEs at different applied potentials. Reproduced with permission.[47] Copyright 2020, Nature Publishing Group. (c) Chemical structure of CoPc. (d) Diagram of the membrane electrode assembly and the cell components. (e) $FE_{(CO)}$ and E_{cell} as a function of current density, with and without phenol additive. Reproduced with permission.[45] Copyright 2019, American Association for the Advancement of Science (AAAS).

withdrawing group (–CN). Moreover, NiPc-OMe can stabilize the *COOH intermediate to improve the selectivity towards CO_2-to-CO conversion. Berlinguette and co-workers reported that commercially available CoPc (Fig. 4c) achieved a current density of 150 mA cm^{-2} with CO selectivity >95% in a flow cell (Fig. 4d) and a CO partial current density of 175 mA cm^{-2} in a two-electrode cell.[45] Using phenol as an additive to the CoPc catalysts can maintain the CO selectivity at a high current density due to the function of phenol as a local pH buffer (*i.e.*, providing protons at a high current density) that reduces the overpotential of CO_2RR and slows the formation of inactive bicarbonate at the electrode interface (Fig. 4d). This report shows that the molecular catalyst could be a competitive candidate for the electrocatalytic reduction of CO_2 to CO with high selectivity at the practical current densities. The performance of the electrocatalysts based on earth-abundant elements for electrochemical CO_2-to-CO conversion in the non-alkaline electrolyte is summarized in Table 1.

3. The second step: convert CO to C_{2+}

The direct electroreduction of CO_2 into C_{2+} products suffers from low activity in non-alkaline electrolyte and poor selectivity.[60] As summarized in section 2, in the first step,

Table 1 The performance of catalysts based on earth-abundant elements for the electroreduction of CO_2 to CO in non-alkaline electrolyte

Electrocatalysts	Electrolyte	Reactor	FE (%)	$J_{(CO)}$ (mA cm^{-2})	Ref.
A-Ni-NSG	1.0 M $KHCO_3$	H-Cell	97	22	42
Cu-APC	0.2 M $NaHCO_3$	H-Cell	92	8.6	48
NiPc-OMe	1.0 M $KHCO_3$	Flow-cell	99.5	300	47
Co-TTCOFs	0.5 M $KHCO_3$	H-Cell	91.3	1.84	49
Fe^{3+}–N–C	0.5 M $KHCO_3$	Flow-cell	90	94	50
C–Cu/SnO_2-0.8	0.5 M $KHCO_3$	H-Cell	93	4.6	51
Ni–N_4–C	0.5 M $KHCO_3$	H-Cell	99	24.8	52
Ni-CNT-CC	0.5 M $KHCO_3$	H-Cell	99	32.3	53
C–Zi_1Ni_4-ZIF-8	1.0 M $KHCO_3$	H-Cell	98	71.5	54
Co–N_2	0.5 M $KHCO_3$	H-Cell	94	18.1	55
Ni/Fe–N–C	0.5 M $KHCO_3$	H-Cell	98	9.5	56
Cu/$Ni(OH)_2$	0.5 M $KHCO_3$	H-Cell	92	4.3	57
ZnN_x/C	0.5 M $KHCO_3$	H-Cell	95	13.62	58
(Cl, N)–Mn/G	0.5 M $KHCO_3$	H-Cell	97	10	59
CoPc	Anion exchange membrane	MEA	95	150	45
Ni-NCB	Anion-exchange membrane	MEA	99	130	41

CO_2-derived CO provides sustainable feedstock in CO electrolysis to enhance the performance for producing C_{2+} products and to circumvent the reaction between the alkaline electrolyte and CO_2. The Cu-based electrocatalyst is the only known material with the ability to reduce CO to C_{2+} products with appreciable performance. Many strategies have been developed towards engineering Cu-based catalysts, such as grain boundary engineering,[61,62] phase engineering,[63] crystal facet engineering,[6,64] and nanostructuring,[65,66] to improve the product selectivity and catalytic activity.

Among the mentioned strategies, much attention has been paid to grain boundary engineering for developing oxide-derived Cu catalysts (OD-Cu) due to their ability of improving the selectivity of C_{2+} products in CO electrolysis.[61,62] Kanan and co-workers reported that OD-Cu catalysts can improve the intrinsic activity towards C_{2+} production in CO electrolysis.[62] OD-Cu electrocatalysts were prepared by annealing polycrystalline Cu foil in air at 500 °C to form a Cu_2O layer on the Cu foil surface and subsequently reducing this oxide layer to metallic Cu. OD-Cu 1 was prepared by the electroreduction of Cu_2O in an aqueous solution at ambient temperature; OD-Cu 2 was obtained *via* the reduction of Cu_2O in H_2 atmosphere at 130 °C. As shown in Fig. 5a, the high-resolution TEM image of the OD Cu 1 catalyst showed distinct grain boundaries. Benefiting from the highly active sites at the grain boundary, OD-Cu achieved multi-carbon oxygenates (ethanol, acetate, and *n*-propanol) with a faradaic efficiency of 57% in CO-saturated alkaline electrolyte (Fig. 5b). Therefore, engineering the grain boundary is a promising strategy to change the intrinsic catalytic property of nanocrystalline materials toward C_{2+} production.

To reveal the effect of the annealing temperature of OD-Cu electrodes, scientists annealed the OD-Cu-500 catalyst (an OD-Cu catalyst obtained by 350 °C air oxidation) under N_2 at 200 and 350 °C in order to promote grain coalescence at a different degree.[61] The TEM image of OD-Cu-500 shows the distribution of grain boundaries in a dense polycrystalline network (Fig. 5c). Upon annealing, the intrinsic activity of OD-Cu for CO reduction was significantly reduced (Fig. 5d). The electrode annealed at 350 °C showed less than 5% faradaic efficiency for CO reduction. The temperature-programmed desorption of CO on OD-Cu revealed the presence of strong CO binding sites on the OD-Cu surface. Strong CO binding may increase the CO coverage on the catalyst surface to enhance the rate of CO reduction. The thermal annealing of OD-Cu electrodes can reduce the proportion of strong-binding sites on the surface, which is responsible for low activity in CO reduction. Xu *et al.* employed *operando* attenuated total reflection surface-enhanced infrared absorption spectroscopy (ATR-SEIRAS) to identify the CO adsorption band on OD-Cu at 2058 cm^{-1}, which is different from those on polycrystalline copper but similar to the CO adsorption band on Cu(100).[67] OD-Cu may have more Cu(100) facets, which are regarded as sites for C–C coupling in CO_2/CO reduction. Unlike the use of Cu_2O as the precursor, Wang and co-worker prepared Cu nanowires by the thermal reduction of CuO nanowires in H_2 at 150–300 °C.[68] Fig. 5e shows the SEM image of Cu nanowires produced by hydrogen reduction at 150 °C (HR-150). The HR-150 Cu nanowires achieved an ethanol FE of 50% and a total FE of 65% for CO reduction at −0.3 V *vs.* RHE (Fig. 5f). The electrosorption of hydroxide (OH_a), temperature-programmed CO desorption, and DFT calculations suggest that the high ethanol selectivity is attributed to the coordinately unsaturated (110) surface sites on the Cu nanowires. Although OD-Cu catalysts can enhance the activity and selectivity of the C_{2+} products, a full picture of the structure–activity relationship that can guide the rational design of catalysts is still missing.

Most studies on CO reduction have been performed in the H-cell with electrocatalysts immersed in CO-saturated aqueous electrolyte, which suffer from mass transport limitations due to the extremely low solubility of CO in aqueous solution (1 mM in 1 bar saturated H_2O).[69] The flow-cell reactor with gas diffusion electrodes (GDE) is designed to circumvent mass transport limitations by directly feeding gaseous reactants to the electrode–electrolyte interface. As shown in Fig. 6a, the triple-phase boundary was formed at the catalyst particles, liquid electrolyte, and gaseous reactants, which can achieve high rates of CO reduction. Jiao *et al.* first used a flow system to achieve high rates for CO reduction using commercial copper particles and OD-Cu particles as the electrocatalysts.[23] The morphology and particle size of commercial micrometer copper and OD-Cu particles are shown in the SEM images (Fig. 6b and c). The CO reduction performances are summarized in Fig. 6d and e. OD-Cu catalysts achieved a C_{2+} selectivity of 91% and a partial current density over 635 mA cm^{-2} in electrochemical CO reduction. This work also compared the performance of CO_2RR and CORR to illustrate the advantages of CO electrolysis for C_{2+} production. Kanan and co-workers employed a membrane electrode assembly cell with GDE and achieved a current density over 100 mA cm^{-2} for the formation of C_{2+} as well as produced 1.1 M acetate at a cell potential of 2.4 V after 24 h electrolysis.[69] To further illustrate the advantages of CO over CO_2 as the reactant for C_{2+} production at high current densities, O. Hinrichsen and co-workers reported the performances of CO_2RR and CORR on gas diffusion electrodes using commercial Cu-powders as the catalyst layer in a flow cell.[25] The results showed that higher current densities for C_{2+} products can be achieved at lower working electrode potentials in CORR compared to CO_2RR. Cu nanoparticles (NPs, 40–60 nm) achieved a C_{2+} FE of 89% at the current density of 300 mA cm^{-2} in galvanostatic CO electrolysis, while 34% FE (300 mA cm^{-2}) was obtained in direct CO_2 electroreduction. Fig. 6f and g show the FE of ethylene on Cu NPs of different sizes at various current densities for CO_2RR and CORR. In CORR, the maximum ethylene FE of 54% was achieved using Cu NPs (40–60 nm) but in CO_2RR, a maximum FE of ethylene of only 32% on Cu NPs (60–80 nm) was achieved. These results demonstrate that the two-step conversion of CO_2 to C_{2+} is definitely deserves to

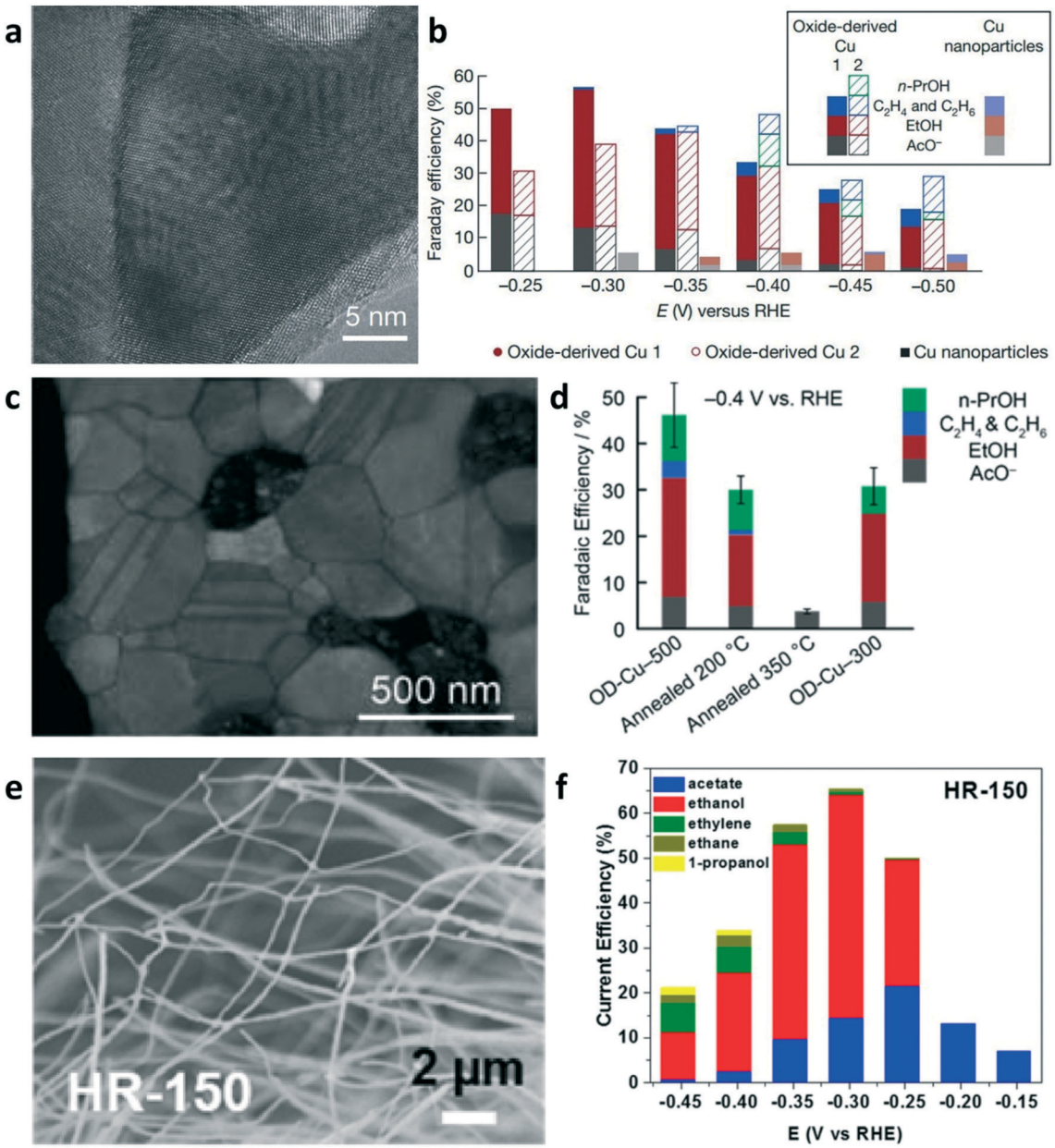

Fig. 5 (a) High-resolution TEM image of the oxide-derived (OD) Cu 1 electrode. (b) FEs of C_{2+} products at various applied potentials. Reproduced with permission.[62] Copyright 2014, Nature Publishing Group. (c) TEM image of OD-Cu-500. (d) FEs of C_{2+} products at −0.4 V *vs.* RHE in CO-saturated 0.1 M KOH. Reproduced with permission.[61] Copyright 2015, American Chemical Society. (e) SEM image of Cu nanowires produced by hydrogen reduction at 150 °C (HR-150). (f) Product distribution of Cu nanowires (HR-150) depending on the electrode potential in CO electrolysis. Reproduced with permission.[68] Copyright 2017, American Chemical Society.

be further explored for any potential application in the industry.

To date, although high FEs of C_{2+} with high current density have been achieved in CO electrolysis, the high selectivity for single multicarbon oxygenate production is still an open challenge. Our group reported freestanding high-quality Cu nanosheets synthesized through solution-phase synthesis.[6] As shown in Fig. 7a, the Cu nanosheets present a two-dimensional (2D) triangular shape morphology with an average edge length of 1.7 ± 0.5 μm. The HRTEM image in Fig. 7b shows that Cu nanosheets selectively expose the Cu(111) surface. As a model catalyst for the electroreduction of CO, highly selective CO-to-acetate conversion was achieved on the Cu nanosheets, with the FE of acetate as high as 48% at an acetate partial current density up to 131 mA cm^{-2} in CO electrolysis (Fig. 7c). Further experimental analysis and computational studies suggested that the high acetate selectivity is due to the suppression of ethylene and ethanol formation, and the acetate formation goes through a ketene intermediate. Jaramillo and co-worker proposed that increasing the roughness factor (RF) of Cu catalysts can be used to increase the rates of C_{2+} production.[70] CuO

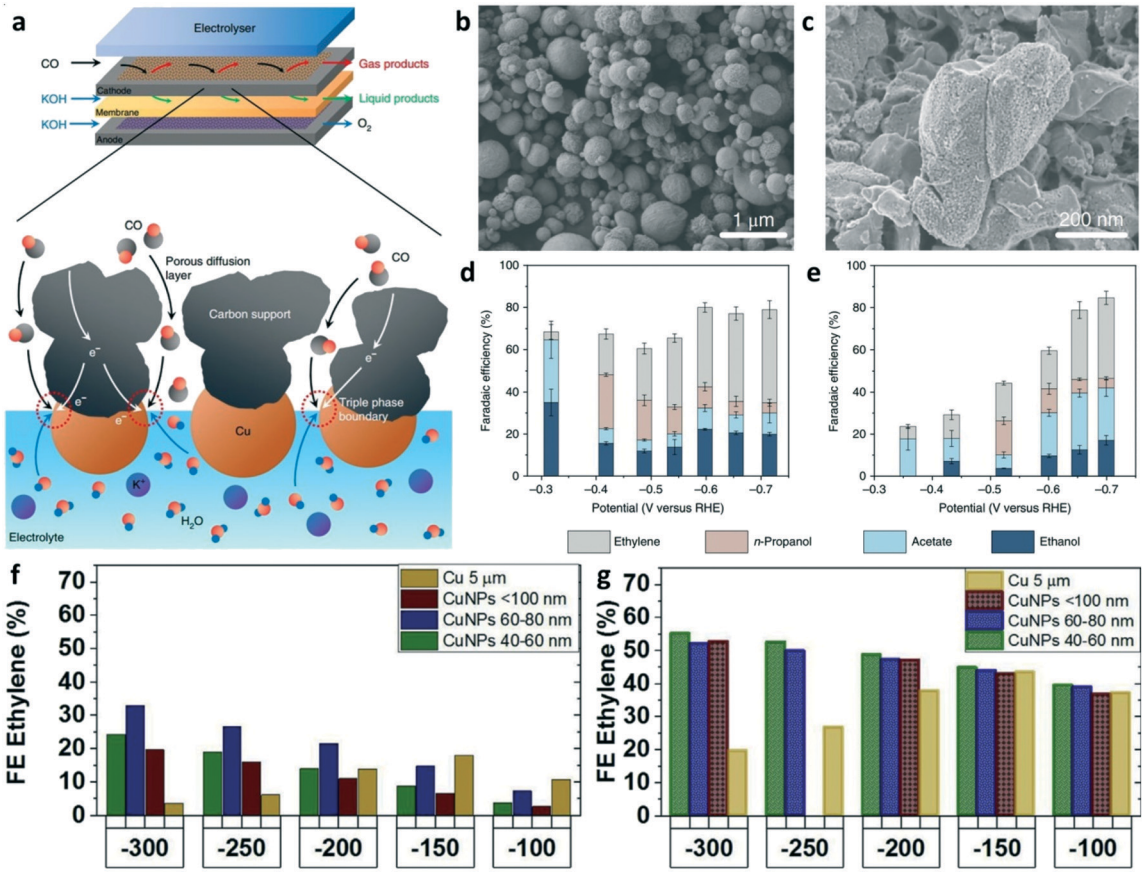

Fig. 6 (a) Schematic illustration of the flow-cell electrolyzer and the triple-phase boundary in the flow-cell reactor. (b) and (c) SEM images of commercial micrometer copper and OD-Cu particles, respectively. (d) and (e) FEs of C_{2+} for OD-Cu and micrometer copper, respectively. Reproduced with permission.[23] Copyright 2018, Nature Publishing Group. (f) FE of ethylene on different sizes of Cu NPs at various current densities for CO_2RR and CORR (g). Reproduced with permission.[25] Copyright 2019, Elsevier.

nanosheets were prepared by oxidizing the surface of a polished Cu foil. The as-synthesized CuO nanosheets were reduced to metallic Cu nanosheets under electrochemical conditions. The TEM images of CuO and Cu nanosheets are shown in Fig. 7d and e, respectively. As shown in Fig. 7f, a maximum FE of 60% was achieved for ethanol formation at −0.33 V *vs.* RHE, which was believed to be benefited by increasing the RF of the Cu catalyst to suppress hydrocarbon and hydrogen production.

The development of catalysts that can convert CO to C_{2+} products with high selectivity at commercially relevant current densities are highly desired, offering more choices for tandem catalyst design in the two-step route of CO_2 to C_{2+} reduction. Undoubtedly, more mechanistic investigations are necessary for the rational design of the catalysts available. The optimization of reactor configurations and increasing the intrinsic activity and selectivity of the electrocatalysts are effective routes for improving the overall performance of CO_2 to C_{2+} conversion.

4. Tandem catalysts

In recent years, tandem catalysis has been extensively explored in thermal heterogeneous catalysis. Tandem catalysis can be achieved on dual catalyst systems or multifunctional catalysts that have more than one type of active site.[27] It is widely accepted that CO is the key intermediate to C_{2+} products in CO_2 electroreduction. Therefore, tandem catalysis can be used in CO_2 electrolysis where CO_2 was converted to CO on the first catalyst or the active site and subsequently reduced to C_{2+} products by the second catalyst or the active site.[24] Cascade (domino) catalysis avoids product separation and stop-and-go operation. Tandem catalysts for CO_2 electrolysis can have a vertically aligned layer-by-layer structure with two catalysts or a single catalyst with more than one type of active site. As discussed in the previous two section, the consideration for CO production and for C–C coupling are necessary to design tandem catalysts.

To rationally control the catalytic selectivity in CO_2RR, Cu–Ag composites with two types of active sites were employed for shifting the selectivity toward the C_{2+} products.[71,72] *Operando* Raman spectroscopy confirmed CO formation on the Ag sites and subsequent CO spillover on the Cu surface for hydrogenation.[71] The Cu–Ag tandem catalysts were prepared by oxide-derived Cu nanowires mixed with Ag nanoparticles. As shown in Fig. 8a, CO was produced on Ag nanoparticles and then spilled to Cu–Ag boundaries for C–C coupling to selectively

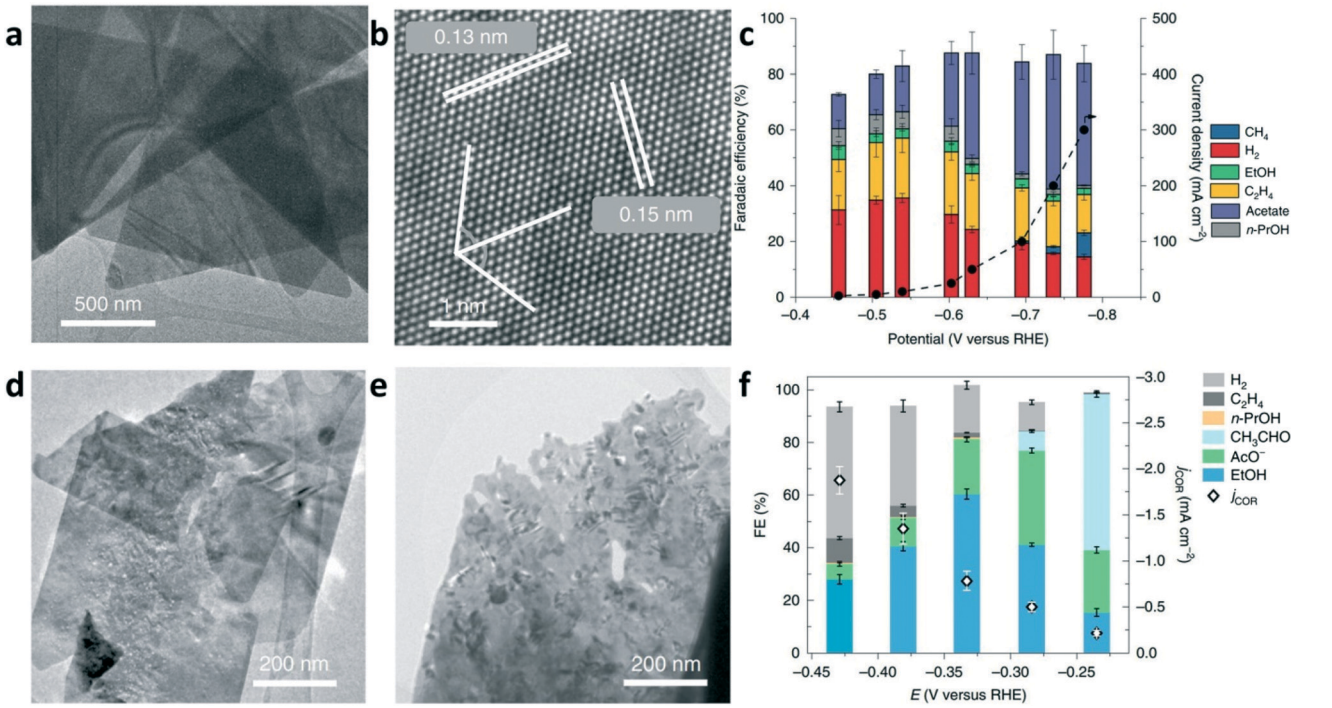

Fig. 7 (a) TEM image and (b) HRTEM of the Cu nanosheets selectively exposing the {111} facets. (c) Total current density and FEs *versus* various applied potentials for CO electrolysis on Cu nanosheets in 2 M KOH. Reproduced with permission.[6] Copyright 2019, Nature Publishing Group. (d) TEM image of representative CuO nanosheets. (e) TEM image of Cu nanosheet after the reduction of CuO nanosheets. (f) FE of products and the geometric current densities for CORR as functions of the applied potential. Reproduced with permission.[70] Copyright 2019, Nature Publishing Group.

generate ethanol.[72] Electrolysis was performed in 0.1 M $KHCO_3$. Compared with the FEs of CO_2RR products on OD-Cu NW (Fig. 8b) and Ag-20 (meaning, Ag NPs with diameter of 20 nm, Fig. 8c), Cu(Ag-20)$_{20}$ (meaning, Cu nanowire/Ag NPs composite at the Ag/Cu nominal molar ratio of 20, Fig. 8d) showed a 5-fold improvement in the ethanol current density. The computational study showed the selective generation of ethanol *via* Langmuir–Hinshelwood *CO + *CH_x (x = 1, 2) coupling at the Cu–Ag boundaries. Sun and co-worker prepared Au–bipy–Cu tandem catalysts by assembled Au NPs on Cu nanowires using 4,4′-bipyridine (bipy) as the linker (Fig. 8e).[73] The TEM image shows that the Au NPs were uniformly dispersed on Cu nanowires (Fig. 8f). CO_2-Saturated aqueous 0.1 M $KHCO_3$ was used as the electrolyte. In addition to the tandem catalytic effect to improve the C_{2+} formation, bipy also promotes the catalytic performance in CO_2 electroreduction. Au–bipy–Cu-1/2 (Au/Cu = 1/2) achieved a CH_3CHO FE of 25%, which is the highest aldehyde selectivity ever reported for CORR and CO_2RR (Fig. 8g). The assembly strategy offers plenty of room for designing tandem catalysts with tunable catalytic selectivity in CO_2RR. Tandem catalysis can also be achieved on multicomponent catalysts with more than one type of active site. Ag_1–$Cu_{1.1}$ (meaning that the mass ratio of Cu to Ag is 1.1) nanodimers (NDs) were prepared by a seeded-growth approach using Ag NPs as the nucleation seeds.[74] The HAADF-STEM image (Fig. 8h) reveals the nanoparticles containing two domains, Ag and Cu. The EDS mapping confirmed a segregated distribution of Ag and Cu in the same nanoparticle (Fig. 8i). The CO_2RR was performed in CO_2-saturated 0.1 M $KHCO_3$ solution. The C_2H_4 FE of ~40% (Fig. 8j) was obtained on the Ag_1–$Cu_{1.1}$ NDs because of tandem catalysis and electronic effects. This work demonstrated that tandem catalysis can be achieved by designing multicomponent catalysts.

Due to its relatively low cost (*vs.* precious metals), commercial ZnO has been explored as a CO-selective catalyst. Inspired by the higher efficiency of the plug flow reactor, Wu and co-workers designed layer-by-layer tandem catalysts with the ZnO catalyst layered on top of the Cu catalyst layer, as shown in Fig. 9a.[75] The Cu–ZnO tandem electrodes were used in a flow-cell with 1 M KOH electrolyte; the CO_2-to-CO conversion occurred on the ZnO catalyst layer and resulted in CO being subsequently reduced to C_{2+} products in the Cu catalyst layer. The rates of C_{2+} products on Cu–ZnO tandem catalysts were superior to those on bare Cu electrode and other Cu- and Zn-based bimetallic catalysts (Fig. 9b). The optimal $Cu_{1.0}/ZnO_{0.20}$ (meaning, the loading of 1.0 mg cm^{-2} Cu and 0.20 mg cm^{-2} ZnO) tandem catalysts exhibited a maximum FE of 78% for C_{2+} products with C_{2+} partial current density up to 466 mA cm^{-2}. The enhanced CO_2-to-C_{2+} yield was attributed to the breaking of the linear scaling relations because of the segregated active sites. This work highlighted the importance of spatial management in tandem catalyst design. Tandem gold on copper electrocatalyst (Fig. 9c) was explored to improve the activity and selectivity towards alcohols in CO_2RR.[76] Electrochemical experiments were performed in 0.1 M $KHCO_3$. As shown in Fig. 9d, the Au/Cu tandem catalyst favored the

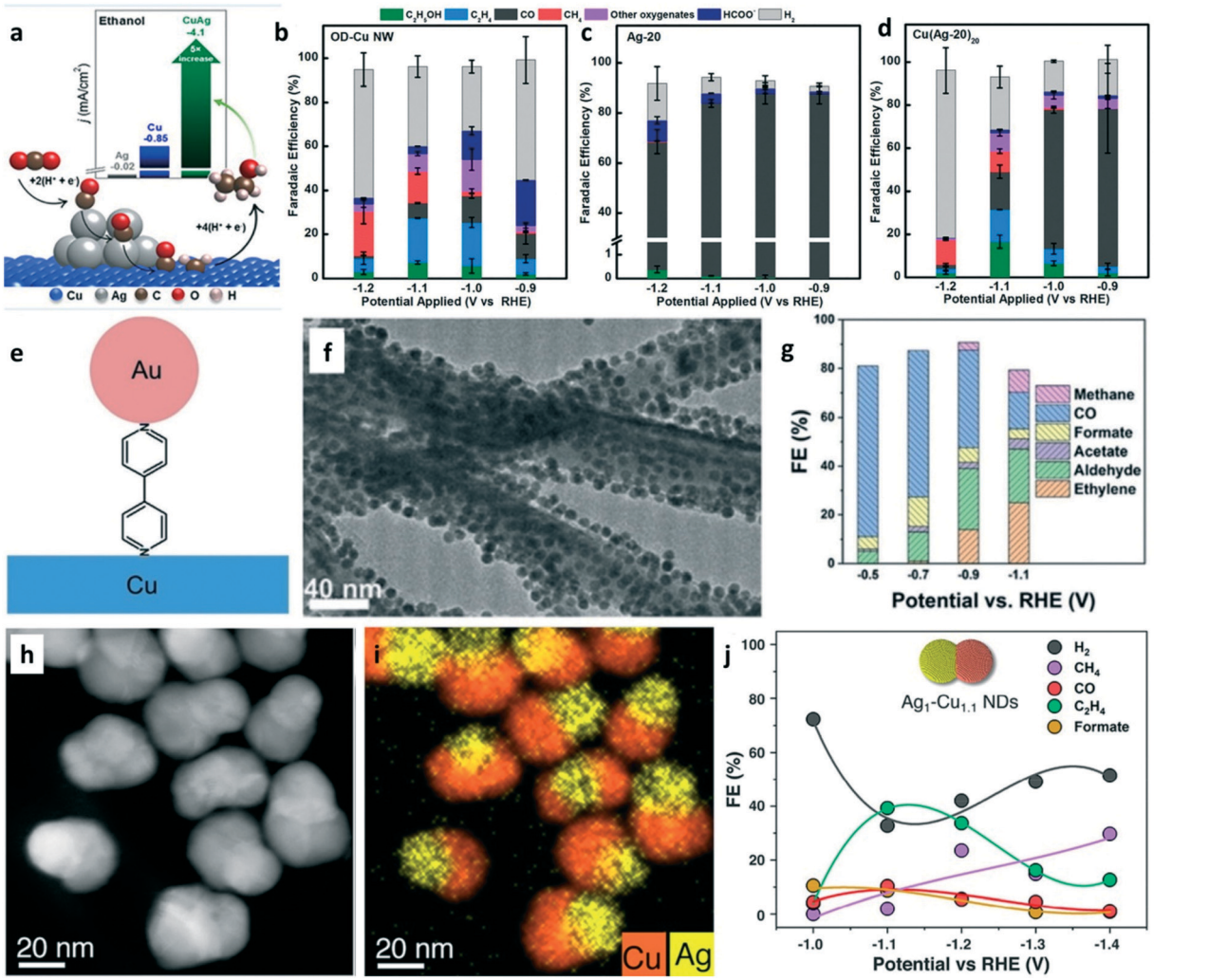

Fig. 8 (a) Schematic illustration of the copper–silver composite for enhancing the selectivity of ethanol. FEs of CO_2RR products on (b) OD-Cu NW, (c) Ag-20, and (d) $Cu(Ag\text{-}20)_{20}$. Reproduced with permission.[72] Copyright 2020, American Chemical Society. (e) Schematic of the Au–bipy–Cu composite catalyst. (f) TEM image of Au–bipy–Cu-1/1. (g) FEs of the products of Au–Cu–bipy catalysts for CO_2RR at various potentials. Reproduced with permission.[73] Copyright 2019, John Wiley and Sons. (h) HAADF-STEM image of Ag_1–$Cu_{1.1}$ nanodimers (NDs). (i) EDX elemental map of Ag_1–$Cu_{1.1}$ NDs. (j) FEs of the CO_2RR products on Ag_1–$Cu_{1.1}$ NDs. Reproduced with permission.[74] Copyright 2019, American Chemical Society.

production of alcohols over hydrocarbons. The rate of CO_2RR to $>2e^-$ products (*i.e.*, excluding HCOOH, CO, and H_2) on the Au/Cu tandem catalyst was over 100 times higher than that on copper at low overpotentials, which may be due to the high local concentration of CO (derived from CO_2–CO conversion on neighboring Au) on the copper surface to accelerate the rate of C–C coupling. Remarkably, the local concentration of CO near the tandem catalyst surface reached its saturation limit, which is difficult to achieve in CO reduction.

As mentioned in section 2, molecular electrocatalysts (*e.g.*, metal phthalocyanine and metal tetraphenylporphyrin) have attracted great attention for CO_2-to-CO conversion. The catalytic performance can be tuned to the electronic structure of the active sites by the ligands and the central metal atoms. As shown in Fig. 10a, the molecule–metal composite was designed by anchoring the molecular complex on the Cu surface.[77] The porphyrin-based metallic complex can efficiently convert CO_2 to CO, which creates the CO-rich local environment for facilitating C–C coupling and even optimizes the reaction pathway for ethanol. Therefore, ethanol FE of 41% (Fig. 10b) and partial current density of 124 mA cm^{-2} (Fig. 10c) were achieved on the FeTPP[Cl]/Cu (meaning, 5,10,15,20-tetraphenyl-21*H*,23*H*-porphine iron(III) chloride was immobilized on the Cu electrode) tandem catalysts at −0.82 V (*vs.* RHE) using 1 M $KHCO_3$ as the electrolyte. This work demonstrated the potential of molecular-complex/copper tandem catalysts to selectively produce C_{2+} products *via* enriched intermediates at the interfaces. Unlike the composites tandem catalysts with multi-sites at the nanoscale mentioned earlier, the layer-by-layer and physical mixture tandem catalysts were also extensively explored in CO_2 electrolysis. The $Cu_{500}Ag_{1000}$ (meaning, the Cu–Ag tandem catalyst with 500 μg cm^{-2} Cu and 1000 μg cm^{-2} Ag) catalyst was prepared by a physical mixture of Cu and Ag nanopowders.[78] The cross-section SEM image of $Cu_{500}Ag_{1000}$ (Fig. 10d) shows

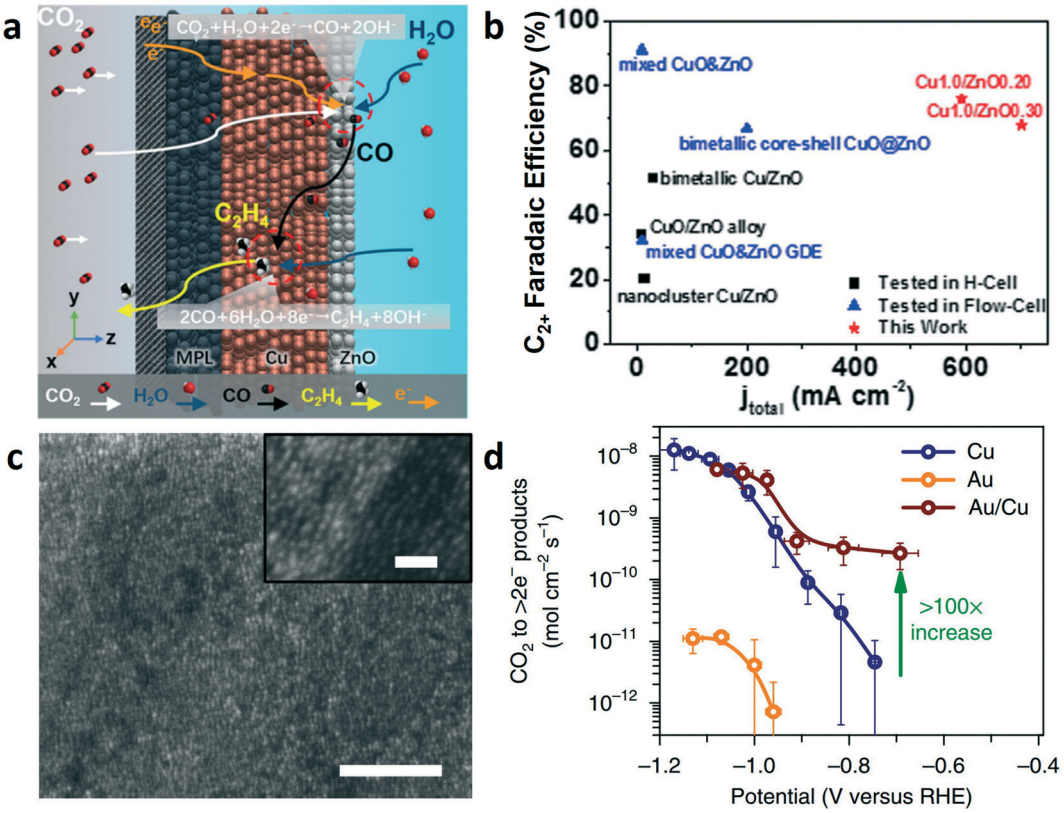

Fig. 9 (a) Schematic illustration of the layered structure of the tandem catalysts in the two-step conversion of CO_2 to C_{2+}. (b) FEs and current densities of C_{2+} on Cu/ZnO tandem catalyst and Cu and ZnO combination catalysts. Reproduced with permission.[75] Copyright 2020, Elsevier. (c) SEM image of the gold nanoparticles on a polycrystalline copper foil (Au/Cu) catalyst, scale bars: 100 nm, insets: 20 nm. (d) Rate of CO_2 reduction to $>2e^-$ products of Au/Cu, copper, and gold catalysts. Reproduced with permission.[76] Copyright 2018, Nature Publishing Group.

that the thickness of the catalyst layer on carbon paper was several microns. The partial current densities of C_{2+} products on the $Cu_{500}Ag_{1000}$ tandem catalysts is 160 mA cm^{-2} at −0.7 V using 1.0 M KOH as the electrolyte, while the partial current densities of C_{2+} products on the Cu_{500} catalysts are only about 37 mA cm^{-2} (Fig. 10e). Interestingly, the partial current densities of C_{2+} products on $Cu_{500}Ag_{1000}$ were much higher than that of Cu_{500} and Ag_{1000}. To analyze the distribution of the C_{2+} product (Fig. 10f), the enhancement factor (EF) was defined by the partial current on tandem $Cu_{500}Ag_{1000}$ divided by that on the Cu_{500} catalyst. Oxygenate products (ethanol and acetate) were favored over ethylene on the $Cu_{500}Ag_{1000}$ tandem catalyst, which was consistent with the previous reports.[31,51] Wu and co-worker designed layer-by-layer Cu–Ag tandem electrodes for efficiently converting CO_2 to C_{2+} products.[79] The structure of the Cu/Ag tandem electrodes is shown in Fig. 10g; the top Ag layer and bottom Cu layer are presented in the EDS elemental maps. The cross-section SEM image shows that the thickness of the catalyst layer is about 2 μm. The performance of CO_2RR was evaluated in 1.0 M KOH. The Cu/Ag (0.8 mg cm^{-2}/0.2 mg cm^{-2}) tandem catalysts achieved the highest C_{2+} FE of 87% at −0.78 V among all the Cu/Ag tandem electrodes and pure Cu electrode (Fig. 10h). It has been proved that the Ni–N–C catalysts are highly active for the production of CO from CO_2 reduction. Therefore, Ni–N–C was used as CO-selective catalyst layers in the tandem electrodes. Fig. 10i shows the cross-sectional SEM image and the EDS mapping images for Cu/Ni–N–C tandem catalysts. The maximum C_{2+} selectivity of Cu/Ni–N–C tandem catalysts is lower than that of Cu/Ag (Fig. 10j). But the optimized Cu/Ni–N–C tandem catalysts achieved an FE of 62% for C_2H_4 with a partial current density of 415 mA cm^{-2}. The Cu-based/molecular-complex and Cu/M–N–C tandem catalysts have plenty of room to explore for improving the selectivity and activity of C_{2+} products in CO_2 electroreduction.

Besides CO_2-to-C_{2+} conversion, CO_2-to-methane (CH_4) production can also be achieved on tandem catalysts. The electrochemical reduction of CO_2 to CH_4 is another promising route for carbon utilization. Recently, Wang and co-workers developed a CoPc/Zn–N–C tandem catalyst for CH_4 production.[80] The HAADF-STEM image (Fig. 11a) of Zn–N–C shows that the single Zn atoms were distributed in the N–C framework. For the CoPc/Zn–N–C tandem catalyst toward CO_2RR, the CO_2 is first reduced into CO on CoPc and then CO spills over onto Zn–N–C for further reduction to CH_4. The CH_4 FE of 18.3% (Fig. 11b) and maximum CH_4 current density of 44.3 mA cm^{-2} (Fig. 11c) were achieved on the tandem catalysts at −1.24 V *vs.* RHE using 1 M KOH as the electrolyte. The high CH_4 production rate was attributed to the CoPc-enhanced availability of *H over adjacent N sites in Zn–N_4.

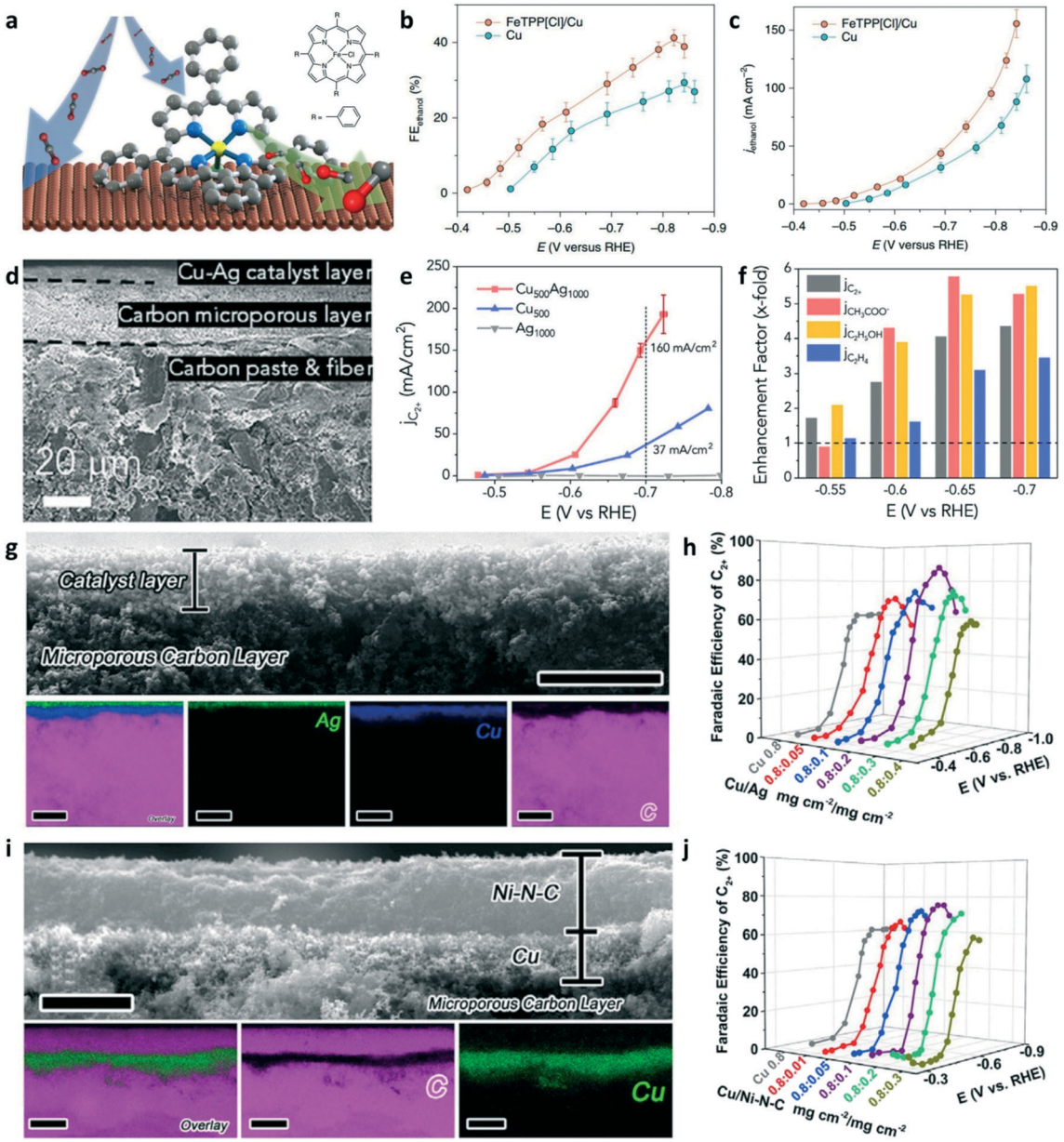

Fig. 10 (a) Schematic illustration of Cu-molecular complexes tandem catalysts for ethanol production. (b) FEs of ethanol on FeTPP[Cl]/Cu and Cu catalysts at various applied potentials. (c) Partial current densities of ethanol on FeTPP[Cl]/Cu and the Cu catalysts. Reproduced with permission.[77] Copyright 2019, Nature Publishing Group. (d) Cross-sectional SEM image of the $Cu_{500}Ag_{1000}$ catalyst supported on carbon paper. (e) The partial current density of C_{2+} products *versus* various applied potentials on $Cu_{500}Ag_{1000}$, Cu_{500}, and Ag_{1000} catalysts. (f) An enhancement factor of total C_{2+} and individual products at various applied potentials on the tandem $Cu_{500}Ag_{1000}$. Reproduced with permission.[78] Copyright 2020, Elsevier. (g) Cross-sectional SEM image (scale bars: 4 μm) and EDS mapping (scale bars: 5 μm) of the Cu/Ag tandem catalyst. (h) FEs of C_{2+} products on various Cu/Ag tandem catalysts. (i) Cross-sectional SEM image and EDS mapping of the Cu/Ni–N–C tandem catalyst. (j) FEs of C_{2+} products on various Cu/Ni–N–C tandem catalysts. Reproduced with permission.[79] Copyright 2020, Elsevier.

CO_2 and CO co-exist at the C–C coupling site of the tandem catalyst but whether the presence of CO promotes the coupling rate of CO_2 is unknown. CuO_x/Ni–N–C tandem catalysts (Fig. 11d) were explored for ethylene production in 0.1 M $KHCO_3$ electrolyte.[81] As shown in Fig. 11e, the C_2H_4 production rates were significantly enhanced when the CO_2/CO mixture was used as the feedstock. The CuO_x/Ni–N–C tandem catalysts were used for CO_2RR by mimicking the CO_2/CO mixture feeding. Interestingly, enhanced C_2H_4 production rates (Fig. 11f) were achieved on CuO_x/Ni–N–C tandem catalysts compared to pure CuO_x NPs. The reason is well-known, *i.e.*, high local CO concentration increases the *CO coverages on the catalysts surface for enhancing the dimerization rates. A modular synthetic approach was proposed to design the tandem catalysts for CO reduction in 0.1 M KOH electrolyte. Thiol-terminated metalloporphyrins were self-assembled on copper electrodes to construct the molecule–metal interfaces (Fig. 11g).[82] The FE of ethanol and

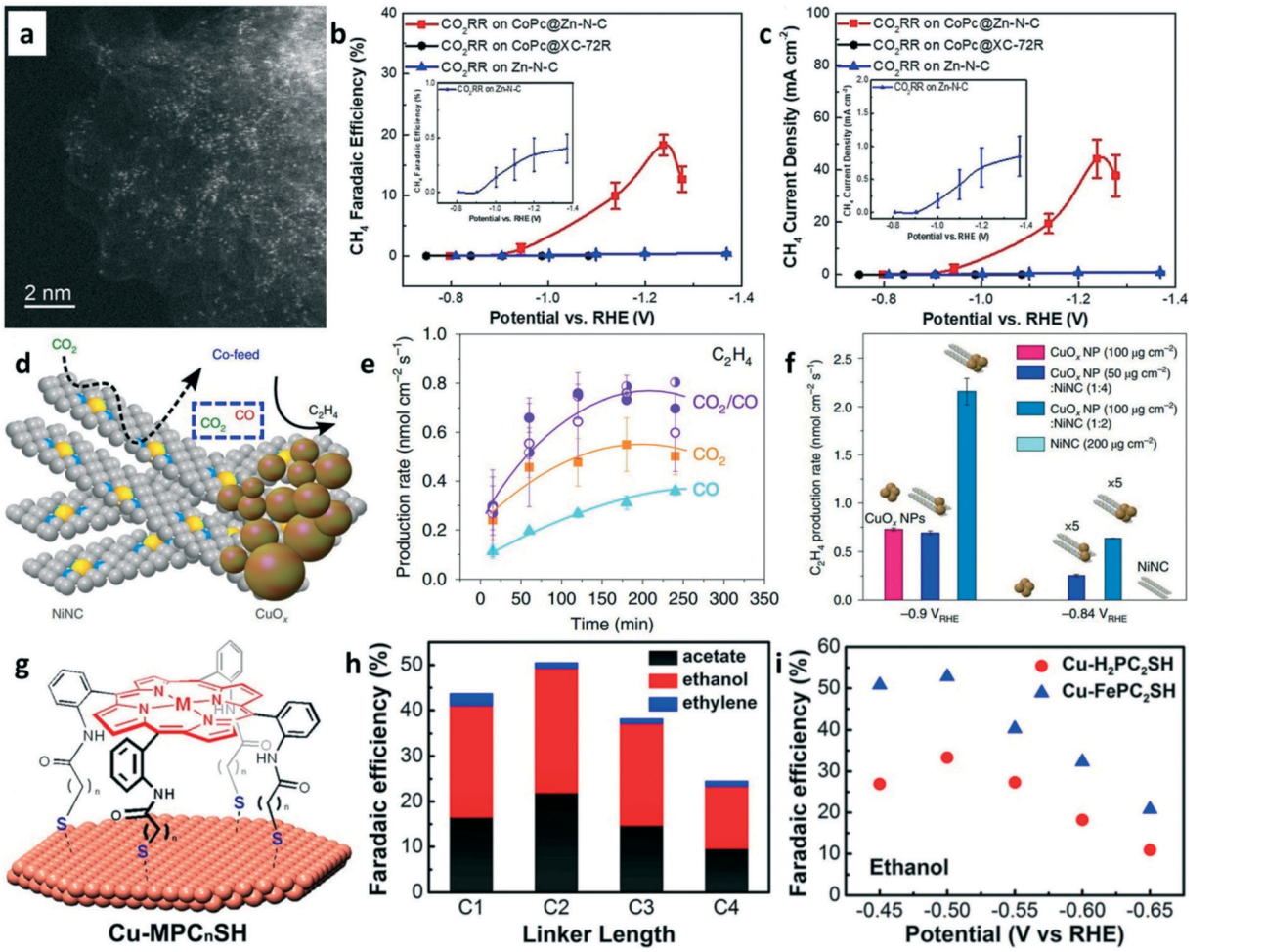

Fig. 11 (a) HAADF-STEM image of Zn–N–C. (b) FEs of CH_4 on different catalysts at various applied potentials. (c) The partial current density of CH_4 on different catalysts at various applied potentials. Reproduced with permission.[80] Copyright 2019, John Wiley and Sons. (d) Schematic of CuO_x–Ni–N–C tandem catalysts for ethylene production. (e) Production rates of ethylene with a different feed ratio of CO_2/CO. (f) Ethylene production rate on different catalysts at various applied potentials. Reproduced with permission.[81] Copyright 2019, Nature Publishing Group. (g) Schematic of the functionalization of Cu surfaces with porphyrin cages. (h) FEs of C_{2+} products on Cu-porphyrin with different linker lengths in CO electrolysis. (i) FEs of ethanol on Cu–H_2PC_2-SH and Cu–$FePC_2SH$ in CO-saturated 0.1 M KOH (aq). Reproduced with permission.[82] Copyright 2017, American Chemical Society.

acetate in CO reduction can be regulated *via* the linker lengths of porphyrin (Fig. 11h). The highest ethanol FE of 52% was obtained on the Cu/$FePC_2SH$ catalyst at −0.5 V *vs.* RHE (Fig. 11i). Although this tandem catalyst was used in CORR, it could be an important model for designing tandem catalysts towards CO_2RR.

The tandem catalysis for CO_2-to-C_{2+} conversion is a powerful approach to close the anthropogenic carbon cycle and the production of chemicals. The tandem catalysis can be achieved on one single particle with more than one type of active site (*e.g.*, Cu–Ag nanodimers), layer-by-layer tandem electrode, physical mixing of different catalysts, and assembly composites (*e.g.*, Au–bipy–Cu). Developing tandem catalysts to improve the formation rates of overall C_{2+} products or a specific C_{2+} product at commercially relevant current densities with high FE are desired for the production of chemicals and storage of renewable electricity. To date, most tandem catalysts have been employed in H-cell and flow-cell for CO_2RR. The MEA-based electrochemical cell uses a solid electrolyte instead of a liquid electrolyte, thus avoiding the further separation of products from the liquid electrolyte. Therefore, the tandem catalysis strategy applied in the MEA electrolyzer may enable CO_2RR implementation in industries.

5. Tandem reaction systems

Unlike the tandem catalysts where the two-step reactions occur in one electrochemical cell, tandem reaction systems were designed to facilitate two-step CO_2 electrochemical reductions in two separate electrochemical cells. As shown in Fig. 12a, CO_2-to-CO conversion occurred in the first flow cell with the Ag catalyst layer, and then the output stream of CO, H_2, and CO_2 (unreacted in the previous step) was separated through the absorption column.[24] The gaseous product output (CO and H_2) from the absorption column was fed into the second electrolyzer using Cu as the catalyst for the production of C_{2+}.

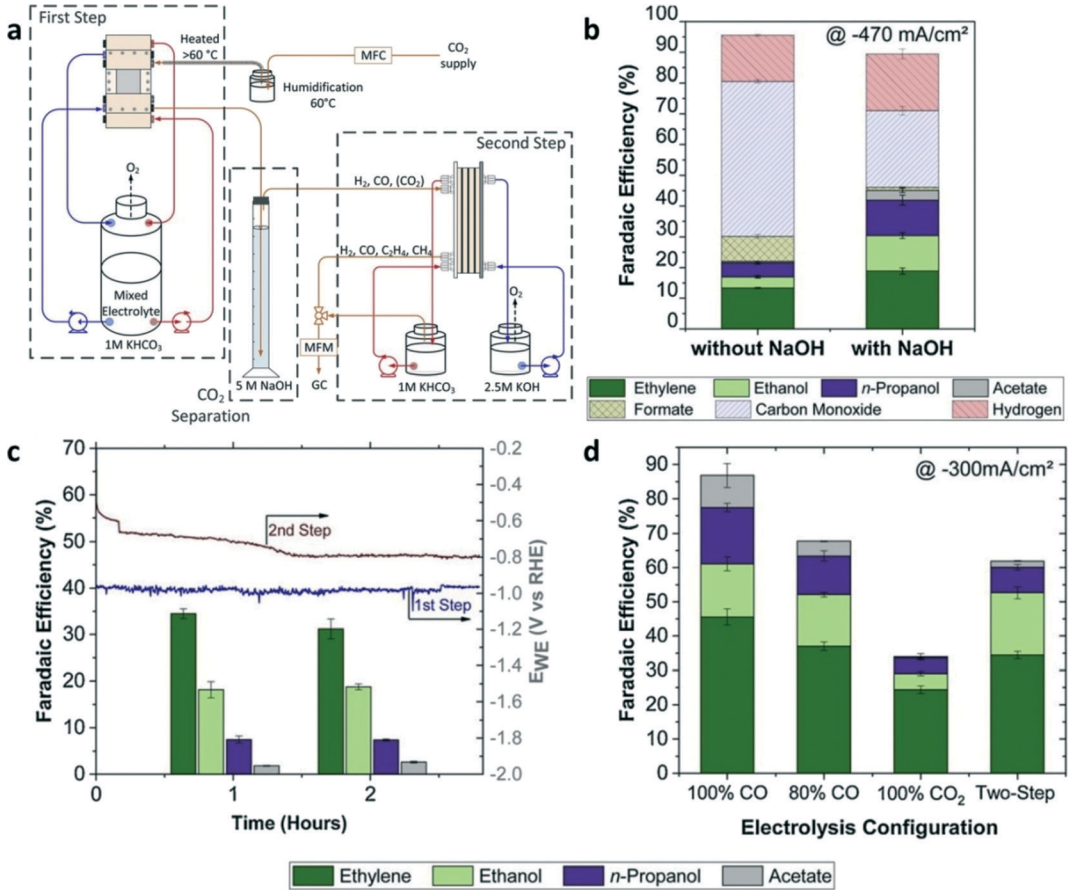

Fig. 12 (a) Schematic illustration of the tandem reaction systems for CO_2RR. (b) FE of the products with or without CO_2 absorption using NaOH as the absorber at a total current density of −470 mA cm^{-2}. (c) FEs of C_{2+} products at the first and second step after 1 and 2 h of CO_2 electrolysis with a total current density of −300 mA cm^{-2}. (d) FEs of C_{2+} products from single-step electrolysis with a different feed ratio of CO_2/CO at a total current density of −300 mA cm^{-2} compared to tandem reaction systems. Reproduced with permission.[24] Copyright 2020, Elsevier.

The two-step reactions were performed in two separated electrolyzers using different electrolytes, the first one (CO_2-to-CO) with a non-alkaline electrolyte and the second one (CO-to-C_{2+}) with an alkaline electrolyte, thus circumventing the problem of consuming hydroxide to form carbonate by CO_2 when an alkaline electrolyte is used for CO_2RR. Whether or not an absorption column is used between two electrolyzers can change the overall performance of CO_2RR. With a CO_2 absorption column, the FE of the C_{2+} product was increased twice compared to that without the absorption step (Fig. 12b). After two hours of electrolysis, the FE of C_2H_4 was slightly decreased while the FEs of ethanol and *n*-propanol remained stable compared with the one hour electrolysis (Fig. 12c). Moreover, CO_2-to-CO conversion at the first step required a higher working electrode potential than that required by CO-to-C_{2+} conversion at the second step. The overall FE of the C_{2+} products obtained from the two-step electrolysis in the tandem reactors was nearly two times higher than that obtained from the single-step electrochemical reduction of pure CO_2 (Fig. 12d).

It was proved that the alkaline electrolyte can improve the selectivity and formation rates of C_{2+} products in CO_2RR and CORR. Therefore, the second step for the reduction of CO to C_{2+} can be performed in alkaline electrolytes to improve the overall performance of CO_2RR in tandem reaction systems. To increase the concentration of CO in the output of the first step, CO-selective catalysts with high single-pass conversion are desired, which can reduce the separation cost and improve the overall performance. Jiao and co-workers optimized the test conditions and achieved maximum single-pass CO_2 conversion. The maximum amount of CO_2 being reduced to CO was limited to 43% in the flow cell.[83]

6. Conclusion and outlook

Herein, we discussed the advantages of the two-step approach for CO_2RR as well as many applicable strategies (*e.g.*, nanostructuring, alloying, phase engineering, grain boundary engineering, and crystal facet engineering) to improve the intrinsic activity of the catalysts for CO_2RR/CORR.[21] To enable the two-step CO_2RR, both tandem catalysis in a single reactor and tandem reactors have been explored. The most important thing is that the two-step approach can avoid the problem of carbonate formation in the alkaline electrolyte, which is a major hurdle in the direct CO_2RR to C_{2+}, while taking the advantage of alkaline electrolytes for promoting the rate of C–C coupling in CO-to-

C_{2+} conversion. To push CO_2RR closer to commercialization, we would like to emphasize the following directions: (1) development of stable copper-based catalysts that can work during long-term operation, (2) optimizing the microstructure of the tandem catalyst and the structure of the tandem electrode for the effective production of C_{2+}, (3) increasing the single-pass CO_2-to-CO conversion, (4) incorporation of a tandem catalysis strategy into MEA-based electrochemical cells to avoid product separation and concentration processes from liquid electrolytes, (5) reactor engineering, and (6) possible coupling of other useful reactions with CO_2RR to produce chemicals.

Chemical production through CO_2RR is not yet competitive to be employed in the petrochemical industry. Due to the fact that fossil fuels on Earth are depleting, the most promising alternative energy system, hydrogen economy, however, does not have the capability to directly provide the necessary daily chemicals that the petrochemical industry is providing. In that case, CO_2RR may be our only option for the sustainable production of necessary chemicals.

Conflicts of interest

There are no conflicts to declare.

Acknowledgements

The authors acknowledge the support from the National Natural Science Foundation of China, under Award 21972016 and 21773023.

References

1 D. F. Gao, R. M. Aran-Ais, H. S. Jeon and B. Roldan Cuenya, *Nat. Catal.*, 2019, **2**, 198–210.
2 Y. Y. Birdja, E. Perez-Gallent, M. C. Figueiredo, A. J. Gottle, F. Calle-Vallejo and M. T. M. Koper, *Nat. Energy*, 2019, **4**, 732–745.
3 M. Aresta, A. Dibenedetto and A. Angelini, *Chem. Rev.*, 2014, **114**, 1709–1742.
4 L. M. Wang, W. L. Chen, D. D. Zhang, Y. P. Du, R. Amal, S. Z. Qiao, J. W. Bf and Z. Y. Yin, *Chem. Soc. Rev.*, 2019, **48**, 5310–5349.
5 Y. J. Sa, C. W. Lee, S. Y. Lee, J. Na, U. Lee and Y. J. Hwang, *Chem. Soc. Rev.*, 2020, **49**, 6632–6665.
6 W. Luc, X. B. Fu, J. J. Shi, J. J. Lv, M. Jouny, B. H. Ko, Y. B. Xu, Q. Tu, X. B. Hu, J. S. Wu, Q. Yue, Y. Y. Liu, F. Jiao and Y. J. Kang, *Nat. Catal.*, 2019, **2**, 423–430.
7 Y. Hori, R. Takahashi, Y. Yoshinami and A. Murata, *J. Phys. Chem. B*, 1997, **101**, 7075–7081.
8 Y. Hori, A. Murata and Y. Yoshinami, *J. Chem. Soc., Faraday Trans.*, 1991, **87**, 125–128.
9 C. T. Dinh, T. Burdyny, M. G. Kibria, A. Seifitokaldani, C. M. Gabardo, F. P. G. de Arquer, A. Kiani, J. P. Edwards, P. De Luna, O. S. Bushuyev, C. Q. Zou, R. Quintero-Bermudez, Y. J. Pang, D. Sinton and E. H. Sargent, *Science*, 2018, **360**, 783–787.
10 A. Loiudice, P. Lobaccaro, E. A. Kamali, T. Thao, B. H. Huang, J. W. Ager and R. Buonsanti, *Angew. Chem., Int. Ed.*, 2016, **55**, 5789–5792.
11 S. L. Chu, X. P. Yan, C. Choi, S. Hong, A. W. Robertson, J. Masa, B. X. Han, Y. S. Jung and Z. Y. Sun, *Green Chem.*, 2020, **22**, 6540–6546.
12 W. Zhang, C. Q. Huang, Q. Xiao, L. Yu, L. Shuai, P. F. An, J. Zhang, M. Qiu, Z. F. Ren and Y. Yu, *J. Am. Chem. Soc.*, 2020, **142**, 11417–11427.
13 B. X. Zhang, J. L. Zhang, M. L. Hua, Q. Wan, Z. Z. Su, X. N. Tan, L. F. Liu, F. Y. Zhang, G. Chen, D. X. Tan, X. Y. Cheng, B. X. Han, L. R. Zheng and G. Mo, *J. Am. Chem. Soc.*, 2020, **142**, 13606–13613.
14 M. Zhong, K. Tran, Y. M. Min, C. H. Wang, Z. Y. Wang, C. T. Dinh, P. De Luna, Z. Q. Yu, A. S. Rasouli, P. Brodersen, S. Sun, O. Voznyy, C. S. Tan, M. Askerka, F. L. Che, M. Liu, A. Seifitokaldani, Y. J. Pang, S. C. Lo, A. Ip, Z. Ulissi and E. H. Sargent, *Nature*, 2020, **581**, 178–184.
15 S. Ma, M. Sadakiyo, M. Heima, R. Luo, R. T. Haasch, J. I. Gold, M. Yamauchi and P. J. A. Kenis, *J. Am. Chem. Soc.*, 2017, **139**, 47–50.
16 S. H. Zhong, X. L. Yang, Z. Cao, X. L. Dong, S. M. Kozlov, L. Falivene, J. K. Huang, X. F. Zhou, M. N. Hedhili, Z. P. Lai, K. W. Huang, Y. Han, L. Cavallo and L. J. Li, *Chem. Commun.*, 2018, **54**, 11324–11327.
17 X. Wei, Z. L. Yin, K. J. Lyu, Z. Li, J. Gong, G. W. Wang, L. Xiao, J. T. Lu and L. Zhuang, *ACS Catal.*, 2020, **10**, 4103–4111.
18 D. Wakerley, S. Lamaison, F. Ozanam, N. Menguy, D. Mercier, P. Marcus, M. Fontecave and V. Mougel, *Nat. Mater.*, 2019, **18**, 1222–1228.
19 D. M. Weekes, D. A. Salvatore, A. Reyes, A. X. Huang and C. P. Berlinguette, *Acc. Chem. Res.*, 2018, **51**, 910–918.
20 C. M. Gabardo, C. P. O'Brien, J. P. Edwards, C. McCallum, Y. Xu, C. T. Dinh, J. Li, E. H. Sargent and D. Sinton, *Joule*, 2019, **3**, 2777–2791.
21 M. Jouny, G. S. Hutchings and F. Jiao, *Nat. Catal.*, 2019, **2**, 1062–1070.
22 J. A. Rabinowitz and M. W. Kanan, *Nat. Commun.*, 2020, **11**, 5231.
23 M. Jouny, W. Luc and F. Jiao, *Nat. Catal.*, 2018, **1**, 748–755.
24 N. S. R. Cuellar, C. Scherer, B. Kackar, W. Eisenreich, C. Huber, K. Wiesner-Fleischer, M. Fleischer and O. Hinrichsen, *J. CO2 Util.*, 2020, **36**, 263–275.
25 N. S. R. Cuellar, K. Wiesner-Fleischer, M. Fleischer, A. Rucki and O. Hinrichsen, *Electrochim. Acta*, 2019, **307**, 164–175.
26 H. Xiao, T. Cheng, W. A. Goddard and R. Sundararaman, *J. Am. Chem. Soc.*, 2016, **138**, 483–486.
27 T. L. Lohr and T. J. Marks, *Nat. Chem.*, 2015, **7**, 477–482.
28 M. J. Climent, A. Corma, S. Iborra and M. J. Sabater, *ACS Catal.*, 2014, **4**, 870–891.
29 R. G. Mariano, K. McKelvey, H. S. White and M. W. Kanan, *Science*, 2017, **358**, 1187–1191.
30 Y. X. Wang, C. Y. Li, Z. X. Fan, Y. Chen, X. Li, L. Cao, C. H. Wang, L. Wang, D. Su, H. Zhang, T. Mueller and C. Wang, *Nano Lett.*, 2020, **20**, 8074–8080.

31 S. Zhao, R. X. Jin and R. C. Jin, *ACS Energy Lett.*, 2018, **3**, 452–462.
32 J. A. Trindell, J. Clausmeyer and R. M. Crooks, *J. Am. Chem. Soc.*, 2017, **139**, 16161–16167.
33 C. Rogers, W. S. Perkins, G. Veber, T. E. Williams, R. R. Cloke and F. R. Fischer, *J. Am. Chem. Soc.*, 2017, **139**, 4052–4061.
34 K. Sun, T. Cheng, L. N. Wu, Y. F. Hu, J. G. Zhou, A. Maclennan, Z. H. Jiang, Y. Z. Gao, W. A. Goddard and Z. J. Wang, *J. Am. Chem. Soc.*, 2017, **139**, 15608–15611.
35 S. Lamaison, D. Wakerley, J. Blanchard, D. Montero, G. Rousse, D. Mercier, P. Marcus, D. Taverna, D. Giaume, V. Mougel and M. Fontecave, *Joule*, 2020, **4**, 395–406.
36 S. B. Liu, H. B. Tao, L. Zeng, Q. Liu, Z. G. Xu, Q. X. Liu and J. L. Luo, *J. Am. Chem. Soc.*, 2017, **139**, 2160–2163.
37 S. Mezzavilla, S. Horch, I. E. L. Stephens, B. Seger and I. Chorkendorff, *Angew. Chem., Int. Ed.*, 2019, **58**, 3774–3778.
38 M. H. Li, H. F. Wang, W. Luo, P. C. Sherrell, J. Chen and J. P. Yang, *Adv. Mater.*, 2020, **32**, 2001848.
39 Y. Cheng, S. Z. Yang, S. P. Jiang and S. Y. Wang, *Small Methods*, 2019, **3**, 1800440.
40 H. L. Liu, Y. T. Zhu, J. M. Ma, Z. C. Zhang and W. P. Hu, *Adv. Funct. Mater.*, 2020, **30**, 1910534.
41 T. T. Zheng, K. Jiang, N. Ta, Y. F. Hu, J. Zeng, J. Y. Liu and H. T. Wang, *Joule*, 2019, **3**, 265–278.
42 H. B. Yang, S. F. Hung, S. Liu, K. D. Yuan, S. Miao, L. P. Zhang, X. Huang, H. Y. Wang, W. Z. Cai, R. Chen, J. J. Gao, X. F. Yang, W. Chen, Y. Q. Huang, H. M. Chen, C. M. Li, T. Zhang and B. Liu, *Nat. Energy*, 2018, **3**, 140–147.
43 N. Corbin, J. Zeng, K. Williams and K. Manthiram, *Nano Res.*, 2019, **12**, 2093–2125.
44 L. Sun, V. Reddu, A. C. Fisher and X. Wang, *Energy Environ. Sci.*, 2020, **13**, 374–403.
45 S. X. Ren, D. Joulie, D. Salvatore, K. Torbensen, M. Wang, M. Robert and C. P. Berlinguette, *Science*, 2019, **365**, 367–369.
46 Y. S. Wu, Z. Jiang, X. Lu, Y. Y. Liang and H. L. Wang, *Nature*, 2019, **575**, 639–643.
47 X. Zhang, Y. Wang, M. Gu, M. Y. Wang, Z. S. Zhang, W. Y. Pan, Z. Jiang, H. Z. Zheng, M. Lucero, H. L. Wang, G. E. Sterbinsky, Q. Ma, Y. G. Wang, Z. X. Feng, J. Li, H. J. Dai and Y. Y. Liang, *Nat. Energy*, 2020, **5**, 684–692.
48 J. Q. Jiao, R. Lin, S. J. Liu, W. C. Cheong, C. Zhang, Z. Chen, Y. Pan, J. G. Tang, K. L. Wu, S. F. Hung, H. M. Chen, L. R. Zheng, Q. Lu, X. Yang, B. J. Xu, H. Xiao, J. Li, D. S. Wang, Q. Peng, C. Chen and Y. D. Li, *Nat. Chem.*, 2019, **11**, 222–228.
49 H. J. Zhu, M. Lu, Y. R. Wang, S. J. Yao, M. Zhang, Y. H. Kan, J. Liu, Y. Chen, S. L. Li and Y. Q. Lan, *Nat. Commun.*, 2020, **11**, 497.
50 J. Gu, C. S. Hsu, L. C. Bai, H. M. Chen and X. L. Hu, *Science*, 2019, **364**, 1091–1094.
51 Q. Li, J. J. Fu, W. L. Zhu, Z. Z. Chen, B. Shen, L. H. Wu, Z. Xi, T. Y. Wang, G. Lu, J. J. Zhu and S. H. Sun, *J. Am. Chem. Soc.*, 2017, **139**, 4290–4293.
52 X. G. Li, W. T. Bi, M. L. Chen, Y. X. Sun, H. X. Ju, W. S. Yan, J. F. Zhu, X. J. Wu, W. S. Chu, C. Z. Wu and Y. Xie, *J. Am. Chem. Soc.*, 2017, **139**, 14889–14892.
53 S. Liu, H. B. Yang, S. F. Hung, J. Ding, W. Z. Cai, L. H. Liu, J. J. Gao, X. N. Li, X. Y. Ren, Z. C. Kuang, Y. Q. Huang, T. Zhang and B. Liu, *Angew. Chem., Int. Ed.*, 2020, **59**, 798–803.
54 C. C. Yan, H. B. Li, Y. F. Ye, H. H. Wu, F. Cai, R. Si, J. P. Xiao, S. Miao, S. H. Xie, F. Yang, Y. S. Li, G. X. Wang and X. H. Bao, *Energy Environ. Sci.*, 2018, **11**, 1204–1210.
55 X. Q. Wang, Z. Chen, X. Y. Zhao, T. Yao, W. X. Chen, R. You, C. M. Zhao, G. Wu, J. Wang, W. X. Huang, J. L. Yang, X. Hong, S. Q. Wei, Y. Wu and Y. D. Li, *Angew. Chem., Int. Ed.*, 2018, **57**, 1944–1948.
56 W. H. Ren, X. Tan, W. F. Yang, C. Jia, S. M. Xu, K. X. Wang, S. C. Smith and C. Zhao, *Angew. Chem., Int. Ed.*, 2019, **58**, 6972–6976.
57 L. Dai, Q. Qin, P. Wang, X. J. Zhao, C. Y. Hu, P. X. Liu, R. X. Qin, M. Chen, D. H. Ou, C. F. Xu, S. G. Mo, B. H. Wu, G. Fu, P. Zhang and N. F. Zheng, *Sci. Adv.*, 2017, **3**, e1701069.
58 F. Yang, P. Song, X. Z. Liu, B. B. Mei, W. Xing, Z. Jiang, L. Gu and W. L. Xu, *Angew. Chem., Int. Ed.*, 2018, **57**, 12303–12307.
59 B. X. Zhang, J. L. Zhang, J. B. Shi, D. X. Tan, L. F. Liu, F. Y. Zhang, C. Lu, Z. Z. Su, X. N. Tan, X. Y. Cheng, B. X. Han, L. R. Zheng and J. Zhang, *Nat. Commun.*, 2019, **10**, 2980.
60 X. Y. Liu, P. Schlexer, J. P. Xiao, Y. F. Ji, L. Wang, R. B. Sandberg, M. Tang, K. S. Brown, H. J. Peng, S. Ringe, C. Hahn, T. F. Jaramillo, J. K. Norskov and K. R. Chan, *Nat. Commun.*, 2019, **10**, 32.
61 A. Verdaguer-Casadevall, C. W. Li, T. P. Johansson, S. B. Scott, J. T. McKeown, M. Kumar, I. E. L. Stephens, M. W. Kanan and I. Chorkendorff, *J. Am. Chem. Soc.*, 2015, **137**, 9808–9811.
62 C. W. Li, J. Ciston and M. W. Kanan, *Nature*, 2014, **508**, 504–508.
63 Y. Chen, Z. X. Fan, J. Wang, C. Y. Ling, W. X. Niu, Z. Q. Huang, G. G. Liu, B. Chen, Z. C. Lai, X. Z. Liu, B. Li, Y. Zong, L. Gu, J. L. Wang, X. Wang and H. Zhang, *J. Am. Chem. Soc.*, 2020, **142**, 12760–12766.
64 K. J. P. Schouten, E. P. Gallent and M. T. M. Koper, *ACS Catal.*, 2013, **3**, 1292–1295.
65 Y. X. Wang, D. Raciti and C. Wang, *ACS Catal.*, 2018, **8**, 5657–5663.
66 E. Bertheussen, T. V. Hogg, Y. Abghoui, A. K. Engstfeld, I. Chorkendorff and I. E. L. Stephens, *ACS Energy Lett.*, 2018, **3**, 634–640.
67 A. S. Malkani, M. Dunwell and B. J. Xu, *ACS Catal.*, 2019, **9**, 474–478.
68 D. Raciti, L. Cao, K. J. T. Liv, P. F. Rottmann, X. Tang, C. Y. Li, Z. Hicks, K. H. Bowen, K. J. Hemker, T. Mueller and C. Wang, *ACS Catal.*, 2017, **7**, 4467–4472.
69 D. S. Ripatti, T. R. Veltman and M. W. Kanan, *Joule*, 2019, **3**, 240–256.
70 L. Wang, S. Nitopi, A. B. Wong, J. L. Snider, A. C. Nielander, C. G. Morales-Guio, M. Orazov, D. C. Higgins, C. Hahn and T. F. Jaramillo, *Nat. Catal.*, 2019, **2**, 702–708.
71 J. Gao, H. Zhang, X. Y. Guo, J. S. Luo, S. M. Zakeeruddin, D. Ren and M. Gratzel, *J. Am. Chem. Soc.*, 2019, **141**, 18704–18714.

72 L. R. L. Ting, O. Pique, S. Y. Lim, M. Tanhaei, F. Calle-Vallejo and B. S. Yeo, *ACS Catal.*, 2020, **10**, 4059–4069.
73 J. J. Fu, W. L. Zhu, Y. Chen, Z. Y. Yin, Y. Y. Li, J. Liu, H. Y. Zhang, J. J. Zhu and S. H. Sun, *Angew. Chem., Int. Ed.*, 2019, **58**, 14100–14103.
74 J. F. Huang, M. Mensi, E. Oveisi, V. Mantella and R. Buonsanti, *J. Am. Chem. Soc.*, 2019, **141**, 2490–2499.
75 T. Y. Zhang, Z. Y. Li, J. F. Zhang and J. J. Wu, *J. Catal.*, 2020, **387**, 163–169.
76 C. G. Morales-Guio, E. R. Cave, S. A. Nitopi, J. T. Feaster, L. Wang, K. P. Kuhl, A. Jackson, N. C. Johnson, D. N. Abram, T. Hatsukade, C. Hahn and T. F. Jaramillo, *Nat. Catal.*, 2018, **1**, 764–771.
77 F. W. Li, Y. G. C. Li, Z. Y. Wang, J. Li, D. H. Nam, Y. Lum, M. C. Luo, X. Wang, A. Ozden, S. F. Hung, B. Chen, Y. H. Wang, J. Wicks, Y. Xu, Y. L. Li, C. M. Gabardo, C. T. Dinh, Y. Wang, T. T. Zhuang, D. Sinton and E. H. Sargent, *Nat. Catal.*, 2020, **3**, 75–82.
78 C. B. Chen, Y. F. Li, S. Yu, S. Louisia, J. B. Jin, M. F. Li, M. B. Ross and P. D. Yang, *Joule*, 2020, **4**, 1688–1699.
79 X. She, T. Zhang, Z. Li, H. Li, H. Xu and J. Wu, *Cell Rep. Phys. Sci.*, 2020, **1**, 100051.
80 L. Lin, T. Liu, J. Xiao, H. Li, P. Wei, D. Gao, B. Nan, R. Si, G. Wang and X. Bao, *Angew. Chem., Int. Ed.*, 2020, **59**, 22408–22413.
81 X. L. Wang, J. F. de Araujo, W. Ju, A. Bagger, H. Schmies, S. Kuhl, J. Rossmeisl and P. Strasser, *Nat. Nanotechnol.*, 2019, **14**, 1063–1070.
82 M. Gong, Z. Cao, W. Liu, E. M. Nichols, P. T. Smith, J. S. Derrick, Y. S. Liu, J. J. Liu, X. D. Wen and C. J. Chang, *ACS Cent. Sci.*, 2017, **3**, 1032–1040.
83 E. Jeng and F. Jiao, *React. Chem. Eng.*, 2020, **5**, 1768–1775.